Giant magnon spin conductivity approaching the two-dimensional transport regime in ultrathin yttrium iron garnet films

X-Y. Wei, O. Alves Santos, C.H. Sumba Lusero, G. E. W. Bauer, J. Ben Youssef, and B. J. van Wees

I. FINITE-ELEMENT MODELLING

We measure magnon transport non-locally by monitoring the voltage in a Pt detector as a function of current a Pt injector. The electrical spin accumulation μ_s (expressed in energy), which is generated by a current I in the injector at the YIG interface reads [S1]

$$\mu_s = 2eI\theta_{\mathrm{Pt}} \frac{l_s}{\sigma_e t w} \tanh \frac{t}{2l_s}, \tag{S1}$$

where e, t, w, θ_{Pt}, l_s and σ_s are the electronic charge, the Pt film thickness, width, spin Hall angle, spin relaxation length, and conductivity of the Pt contact. With parameters in Table I the charge current to spin accumulation conversion coefficient $\eta_{\mathrm{inj}} = \mu_s/(eI) = 0.05\,\Omega$ when $w = 400\,\mathrm{nm}$ and $0.21\,\Omega$ when $w = 100\,\mathrm{nm}$.

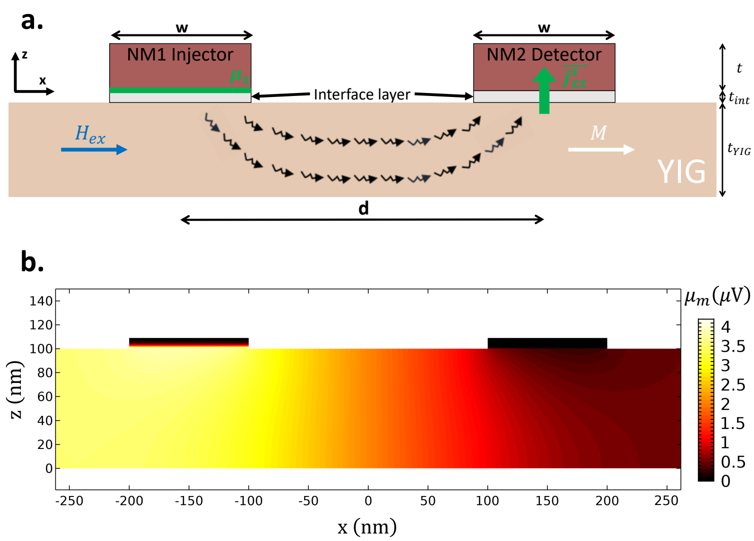

FIG. S1. **a)** The sample configuration and its dimensions in the model simulations. Eq. S1 and Eq. S4 describe the spin accumulation μ_s at the interface, used as input of the model, and the voltage build up in the detector, respectively. **b)** The magnon chemical potential profile for a 100 nm thick YIG film with a charge current $I = 20\,\mu\mathrm{A}$ and 100 nm wide injector/detector contacts and parameters in Table. I. Magnon absorption by the detector electrode causes the dark region close to the detector.

We calculate the diffusive magnon spin transport in YIG films numerically by finite-element method (FEM) [S2] in the configuration of Figure I a) using the COMSOL MULTIPHYSICS (version 5.4) software package. Since the length of the strips is much longer than the electrode separation, we use a 2D model, where the parameters depend on x and z only.

Ohm's Law for magnon current density $\mathbf{j}_m$ in YIG is

$$\mathbf{j}_m = -\sigma_m \nabla \mu_m / e. \tag{S2}$$

where $\nabla = \hat{\boldsymbol{x}}\partial_x + \hat{\boldsymbol{z}}\partial_z$ and σ_m is the magnon spin conductivity. The local magnon current is proportional to $\nabla\mu_m$. The diffusion equation

$$\nabla^2 \mu_m = \frac{\mu_m}{l_m^2}, \tag{S3}$$

governs the magnon chemical potential μ_m, where l_m is the magnon relaxation length. We use the zero-current boundary condition $(\nabla \cdot \boldsymbol{n})\,\mu_m = 0$ for the bottom as well as top surface that is not covered by Pt, where $\boldsymbol{n}$ is the surface normal.

TABLE I. Parameters used to obtain the results in Figure I b) and Figure S2 b) and c).

Parameter	Symbol	Value
Magnon spin conductivity	σ_m	5×10^5 S/m (for 210 nm thickness YIG [S2])
Magnon spin relaxation length	l_m	5×10^{-6} m
Effective spin mixing conductance	G_s^{eff}	2×10^{12} S/m^2
Pt spin Hall angle	θ_{Pt}	0.11
Pt conductivity	σ_e	2×10^6 S/m
Pt spin relaxation length	l_s	1.5×10^{-9} m

The spin accumulation in the detector generates an magnon transport driving force proportional to $\partial\mu_s/\partial z$ that leads to a measurable voltage by the integral over the cross-section $A = wt$

$$V_{\mathrm{nl}} = \frac{\theta_{\mathrm{Pt}}}{2A} \int_A \frac{\partial \mu_s}{\partial z} dA. \tag{S4}$$

The non-local resistance $R_{\mathrm{nl}} = V_{\mathrm{nl}}/(IL)$ (in unit of Ω/m) can be compared with the experimental results. The detector efficiency is the same as that of the injector, $\eta_{\mathrm{det}} = \eta_{\mathrm{inj}}$.

The conversion of spin accumulation in Pt into magnons in YIG is governed by an effective spin conductance G_s^{eff}, which is a certain fraction, ≈ 0.06, of the spin mixing conductance [S3, S4]. It can be modelled by a hypothetical spacer between Pt and YIG with conductivity $\sigma_s^{\mathrm{int}} = G_s^{\mathrm{eff}} t_{\mathrm{int}}$, where $t_{\mathrm{int}} = 1$ nm is the spacer layer thickness.

Figure I b) shows the magnon chemical potential profile μ_m in a 100 nm thick YIG under a charge current of $I = 20\,\mu$A. Injector and detector with $w = 100\,\mathrm{nm}/t = 8\,\mathrm{nm}$ have a center-to-center distance of 300 nm. Table I lists the parameters used to produce Figure Ib). The Pt detector strip acts as a spin sink, absorbing magnons and producing a dark YIG region at the bottom of the detector in Fig. Ib).

II. YIG FILM THICKNESS DEPENDENCE

We measured the non-local resistance in many samples in order to obtain the YIG film thickness and contact-distance dependence. Figure S2 a) shows the experimental results for the non-local resistance for 400 nm wide injector/detector, with center to center distance $d = 2.5\,\mu$m, and for different YIG thicknesses t_{YIG}. We distinguish two regimes: when $t_{\mathrm{YIG}} > l_m$, $R_{\mathrm{nl}}^{1\omega}$ saturates at a small value that does not depend on t_{YIG} anymore. On the other hand, $R_{\mathrm{nl}}^{1\omega}$ increases with decreasing YIG thickness when $t_{\mathrm{YIG}} < l_m$, where l_m is the magnon relaxation length.

Figure S2 b) shows that the non-local resistance calculated with a constant magnon spin conductivity *decreases* when the YIG film become *thinner*. Figure S2 c) shows the results for selected d as a function of t_{YIG} that in contrast to experiments, show a completely different thickness dependence.

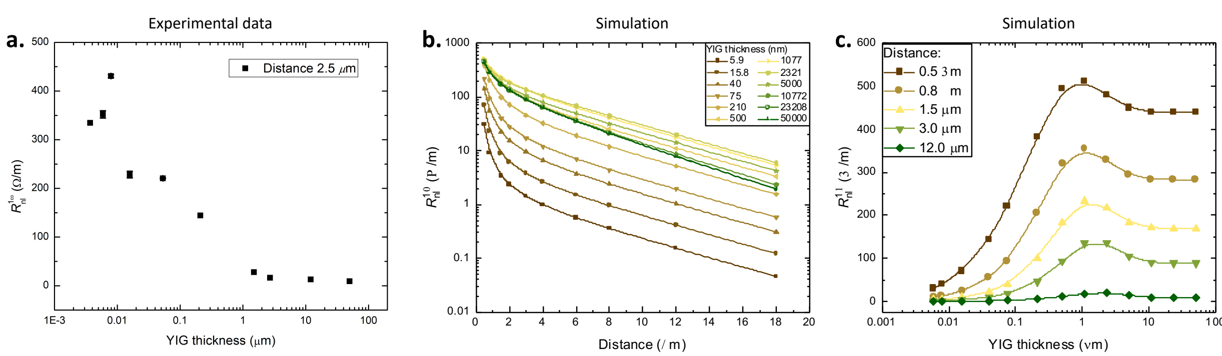

FIG. S2. **a)** YIG thickness dependence of the measured non-local signal $R_{\mathrm{nl}}^{1\omega}$ for a injector/detector distance of $d = 2.5\,\mu$m. **b)** Finite element model results with fixed magnon conductivity $\sigma_m = 5 \times 10^5$ S/m obtained previously for $t_{\mathrm{YIG}} = 210\,\mathrm{nm}$ [S2]. **c)** $R_{\mathrm{nl}}^{1\omega}$ thickness dependency for different distances, for a fixed value of magnon spin conductivity. This shows an opposite trend in comparison with **a)**.

In Figure S2 c), $R_{\mathrm{nl}}^{1\omega}$ saturates above $t_{\mathrm{YIG}} > l_m$ because the magnon current distribution does not change anymore when increasing t_{YIG}. When $t_{\mathrm{YIG}} < l_m$, on the other hand, the non-local resistance vanishes when $t_{\mathrm{YIG}} = 0$, clearly is opposite to the experimental trend. We have to conclude that σ_m dramatically increases the thin-film limit.

We now use σ_m as a single adjustable parameters that fits the experimental results. The numerical simulations are summarized in Figure S3 a) to j). The values of spin relaxation length used in the simulations, shown in Table II, were obtained from the experimental measurements at large distances, where the exponential decay is dominant[S5, S6].

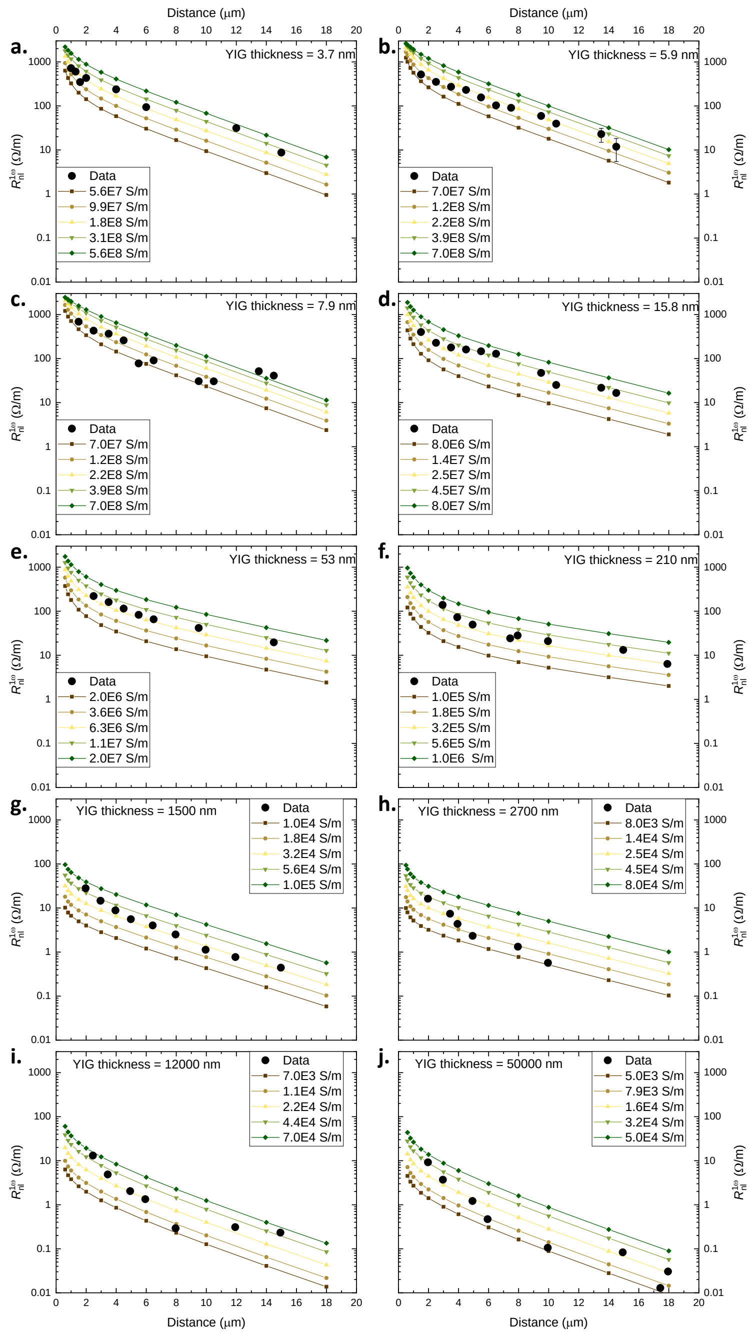

FIG. S3. Comparison between experimental data (black circles) and the two-dimensional diffusive model obtained for different values of the magnon spin conductivity σ_m, (lines brown to green). **a)** to **j)** present the distance dependence of the non-local resistance for different YIG thickness, from 3.7 nm up to 50 μm, indicated on the top of each figure. Based on that comparison we obtain the value of the magnon spin conductivity presented in Figure 5 of the main text.

Each black circle in Figure S3 is an independent measurement and susceptible to variations in the individual sample parameters. It is clear from Figure S3 that the experiments can be well fitted by a σ_m that depends on $t_{\rm YIG}$.

TABLE II. Values of the magnon spin relaxation length adopted in the simulations.

YIG thickness [nm]	Spin relaxation length [μm]
5.9 / 7.9 / 15.8	3.5
53	6.0
210	9.2
1500	4.0
2700	3.5
12000 / 50000	4.0

III. PT|YIG INTERFACE SPIN RESISTANCE

The low interface magnon resistance resulting from the large effective spin mixing conductance makes the Pt strips act as a good spin source/sink. Figure S4 shows the calculated values of non-local resistance for wide range of effective spin conductance, G_s^{eff}. A significant change in the non-local resistance occurs only when we suppress G_s^{eff} to below 2×10^{12} S/m^2. This value is lower than reported by Kohno et. al., 8.8×10^{12} S/m^2[S7] (after local annealing). In Figure S4, a higher G_s^{eff} does not significantly change the calculated non-local resistance, which represents that the giant increase of the non-local resistance we observed is not due to the increase of G_s^{eff}. Figure S5 shows an equivalent circuit model omitting magnon relaxation. The spin current passing through the circuit is dominated by the spin conductance of YIG since $R^s_{\mathrm{int}} < R^s_{\mathrm{YIG}}$. Therefore, R^s_{int} can be disregarded and the magnon transport measured by R_{nl} is determined by the magnon spin conductivity of YIG rather than the YIG|Pt interface conductance.

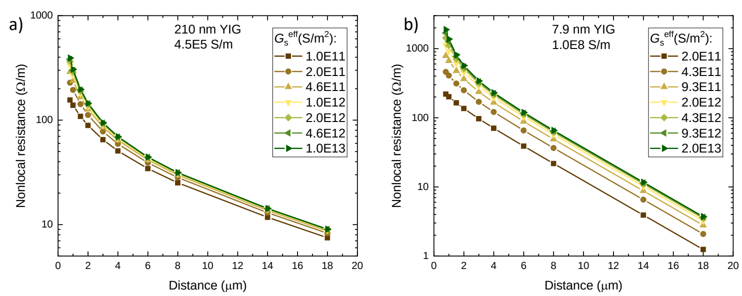

FIG. S4. Calculated non-local resistance for a range of values of the effective spin conductance G_s^{eff} of a 400 nm wide injector/detector. **a)** $t_{\mathrm{YIG}} = 210$ nm, and **b)** $t_{\mathrm{YIG}} = 7.9$ nm YIG. In both cases, a significant change in the magnon transport only occurs for $G_s^{\mathrm{eff}} < 2 \times 10^{12}$ S/m^2.

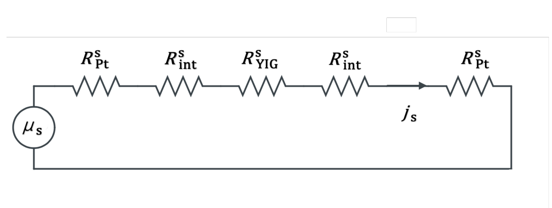

FIG. S5. This equivalent circuit model includes the relevant electronic and magnonic spin resistances and it is valid for short distance (within the magnon relaxation length). μ_s is the spin accumulation induced by the spin Hall effect. R^s_{Pt} is the spin resistance of the Pt strip (injector/detector). R^s_{int} is the interface spin resistance of Pt|YIG. j_s is the electronic spin current injected into the detector, and R^s_{YIG} is the spin resistance of YIG, which is the parameter of interest obtained from the two-dimensional model.

In an additional experiments we placed a third Pt strip between the injector and detector contacts. By absorbing magnons, the middle strip suppresses the non-local signal by a factor of 5 when $d = 2$ μm and $t_{\mathrm{YIG}} = 7.9$ nm, and by a factor of 2 for $d = 4\ \mu$m and $t_{\rm YIG} = 53$ nm. From this, we obtain a best fit with $G_s^{\rm eff} \approx 2.5 \times 10^{12}$ S/m^2 for $t_{\rm YIG} = 7.9$ nm, and $G_s^{\rm eff} \approx 1.0 \times 10^{12}$ S/m^2 for $t_{\rm YIG} = 53$ nm. We therefore adopted $G_s^{\rm eff} = 2 \times 10^{12}$ S/m^2 as the standard value for the effective spin conductance in the other simulations.

We confirm the high $G_s^{\rm eff}$ by comparing results for different widths of the injector/detector contacts. The non-local resistance from the Series B devices in Figure S6 with width $w = 100$ nm, is roughly 10 times higher than that of Series A devices with $w = 400$ nm, which is mainly due to the higher values of the injector/detector conversion efficiency, Eq. S1. The simulations show that when $G_s^{\rm eff}$ is large, magnons are injected/absorbed predominantly in/by only part of the interfaces, i.e., the magnon chemical potential in the YIG film covered by the Pt strip decays according to an absorption length $L_{\rm absorb} = \sqrt{\sigma_m t_{\rm YIG}/G_s^{\rm eff}}$ as sketched in Figure S7 b) in terms of the interface chemical potential μ_m and spin current, $\vec{J}_s$, in the Pt detector. Figure S7 a) shows the calculated resistance for $G_s^{\rm eff} = 2 \times 10^{12}$ S/m^2, $\sigma_m = 1 \times 10^8$ S/m, $t_{\rm YIG} = 3.7$ nm and therefore $L_{\rm absorb} = 430$ nm that agrees with observations. This confirms our value for $G_s^{\rm eff}$ even for the thinnest films.

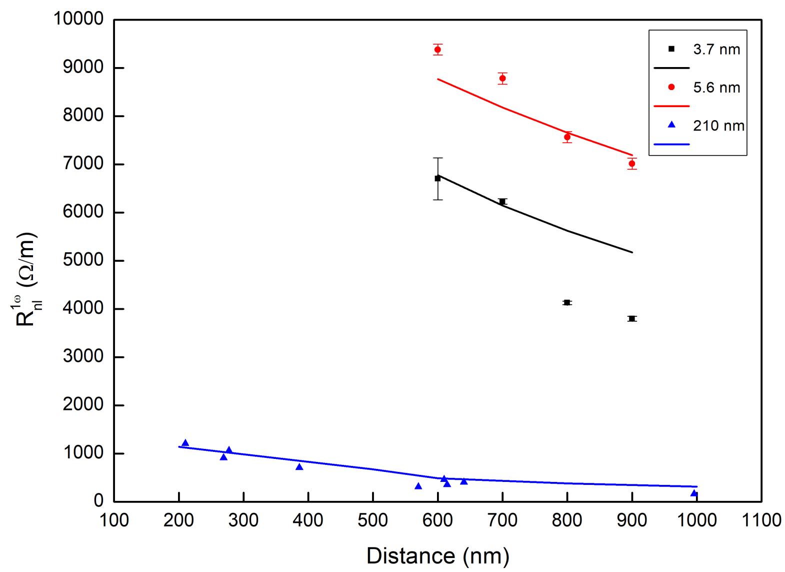

FIG. S6. Non-local resistance as a function of injector-detector separation distance for series B devices. The thickness of YIG films is 3.7 nm and 210 nm. The non-local resistance of 3.7 nm thickness YIG is more than ten times larger than that in 210 nm thickness YIG at same center-to-center distance. The lines are the simulation results based on a 2D-FEM model. The magnon conductivities σ_m here are 1.0×10^8 S/m for 3.7 nm, 1.45×10^8 S/m for 5.6 nm and 4.5×10^5 S/m for 210 nm thickness YIG.

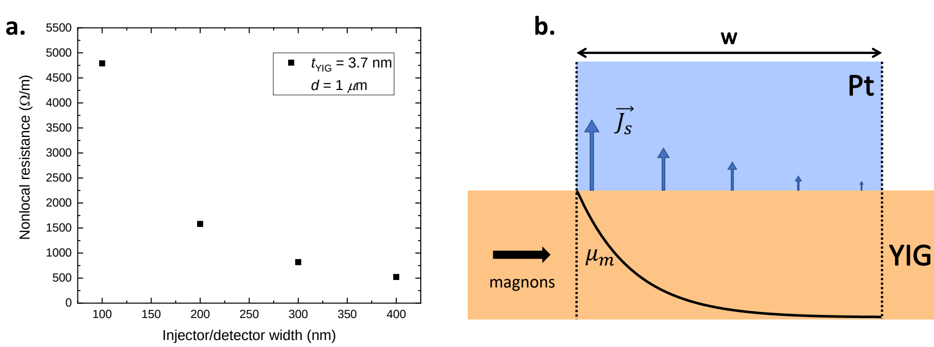

FIG. S7. **a)** Simulation for the non-local resistance with different injector/detector width on 3.7 nm thickness YIG. The center-to-center distance between the injector and the detector is 1 μm. The simulations in Figure S7 are in agreement with the experimental results in Figure S6. **b)** Schematic illustration of the decay of the magnon chemical potential decay and spin current over the Pt width.

IV. MAGNETIC PROPERTIES OF THE YIG FILMS

Table. III summarizes the magnetic properties of the YIG films are determined by broadband ferromagnetic resonance in the range of 2-40 GHz. The magnon spin relaxation lengths obtained by fitting Eq. 3 in the main text, are shown in Figure. S8.

TABLE III. Magnetic properties of the YIG films by FMR characterization.

YIG thickness t_{YIG} (nm)	Gilbert damping α (10^{-4})	Effective field $H_{\mathrm{eff}} = H_{\mathrm{k}} - 4\pi M_{\mathrm{s}}$ (Oe)	Inhomogenous linewidth ΔH_{inh} (Oe)
3.7	5 ± 2.1	1720	17
5.6	not available	1900	not available
5.9	10 ± 2.4	1950	43
7.9	6.3 ± 4.6	1930	53
15.8	0.6 ± 0.5	1960	7.9
53	1.0 ± 0.2	1810	53

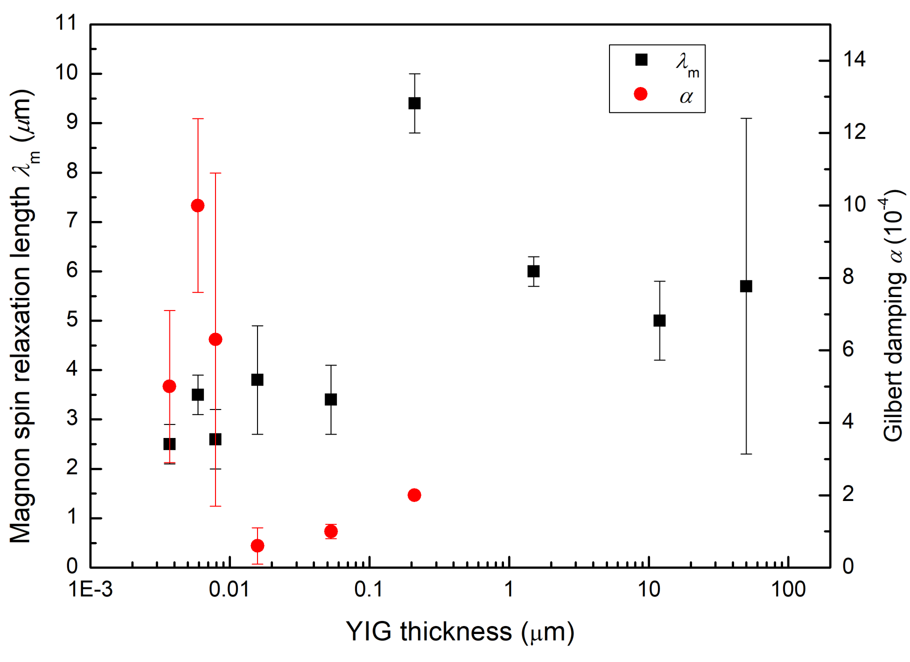

FIG. S8. Magnon spin relaxation length and Gilbert damping parameter as a function of YIG film thickness. The thickness of YIG films ranges from 3.7 nm to 50000 nm (shown on a logarithmic scale). The results from 210 nm to 50000 nm thickness samples are adopted from Cornelissen et al.[S5] and Shan et al.[S6]. The Gilbert damping parameter of the YIG films is also presented here. Note that for ultrathin YIG (around 10 nm), the magnon spin relaxation lengths are similar to each other but the Gilbert damping parameters are quite different.

V. THE SECOND HARMONIC NON-LOCAL RESISTANCE

The second harmonic signal in the non-local resistance is a measure of the thermal spin generation in the magnetic film by the spin Seebeck effect. Figures. S9 a) shows results for this $R_{\mathrm{nl}}^{2\omega}$ (α) as a function of the direction of in-plane magnetic field. $R_{\mathrm{nl}}^{2\omega}$ can be extracted by

$$R_{\mathrm{nl}}^{2\omega}(\alpha) = 1/2R_{\mathrm{nl}}^{2\omega}\cos\alpha + R_{0}^{2\omega}, \tag{S5}$$

where α is the in-plane angle of $\mathbf{H}_{\mathrm{ex}}$ with the x-axis. $R_{0}^{2\omega}$ is an offset signal, possibly by an unintended conventional Seebeck voltage in the detector[S8]. We plot the observed amplitude $R_{\mathrm{nl}}^{2\omega}$ as a function of contact separation in Figures. S9 b) for t_{YIG} = 5.9 nm, 7.9 nm, 15.9 nm (series A with 400 nm wide injector/detector strips). $R_{\mathrm{nl}}^{2\omega}$ in ultrathin YIG is significantly reduced compared to that in thicker YIG films[S5, S6, S9], because the generation of thermal magnons by SSE due to the vertical temperature gradient become less effective. Figures. S9 b) show neither a simple Ohmic or exponential decay as a function of d, which indicates that the generation and transport of magnons is complex and requires detailed modelling of the temperature profile. Just like the magnon conductivity, the spin Seebeck coefficient should also depend on t_{YIG}. A reliable extraction of both parameters as a function of thickness from the second harmonic signals appears impossible at this this time.

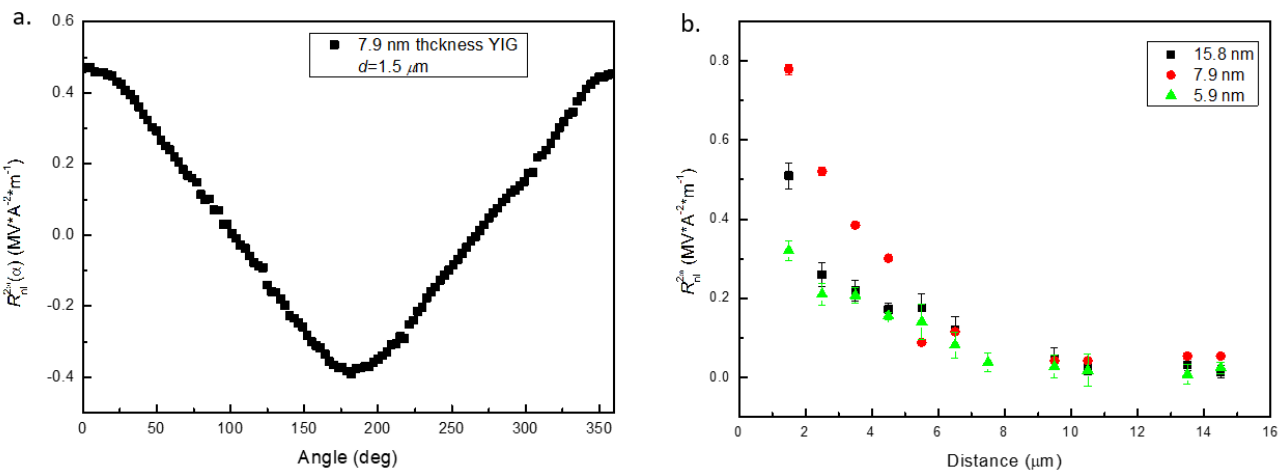

FIG. S9. The second harmonic non-local signals of ultrathin YIG films. **a)** The angle-dependence for t_{YIG} = 7.9 nm and center-to-center distance of injector and detector d = 1.5 μm. **b)** Amplitude of the non-local signals as a function of d for the samples from series A.

VI. MAGNETIC FIELD DEPENDENCE OF THE NON-LOCAL SIGNAL IN ULTRATHIN FILMS

We measured the non-local transport in the series A devices with t_{YIG} = 5.9 nm (Figure. S10) and t_{YIG} = 7.9 nm (Figure. S11) as a function of the strength of a magnetic field along x (in-plane, normal to the contacts). We use Eq. 3 from the main text to extract the field-dependence of the magnon conductivity and relaxation length, as shown in Figure. S12 and Figure. S13, where we use $\eta_{\mathrm{cs}} = \eta_{\mathrm{sc}} = 0.05\,\Omega$ from Section I.

While the magnon spin relaxation length only slightly decreases, the increasing field suppresses the magnon spin conductivity stronger for the thinner samples. This is in line with the dominance of the lowest magnon subband in the thinnest samples, which is more susceptible to magnetic freeze-out of the thermal magnon population.

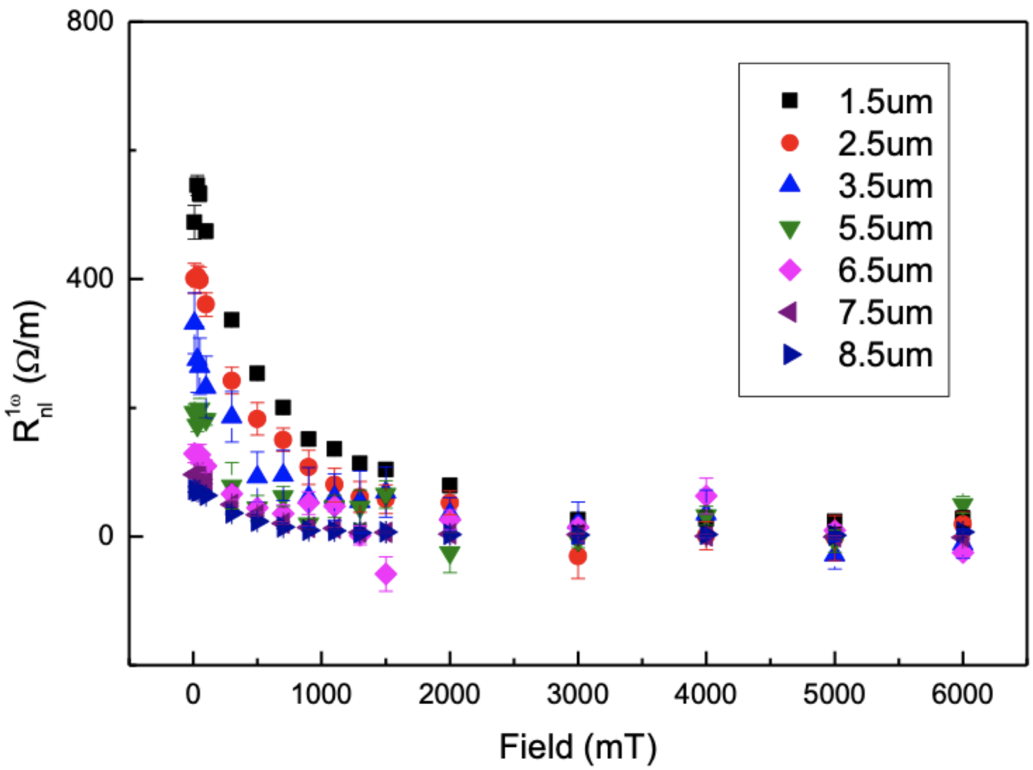

FIG. S10. The non-local resistance $R_{\rm nl}^{1\omega}$ as a function of magnetic field and contact distance of the A series sample with $t_{\rm YIG}$ = 5.9 nm.

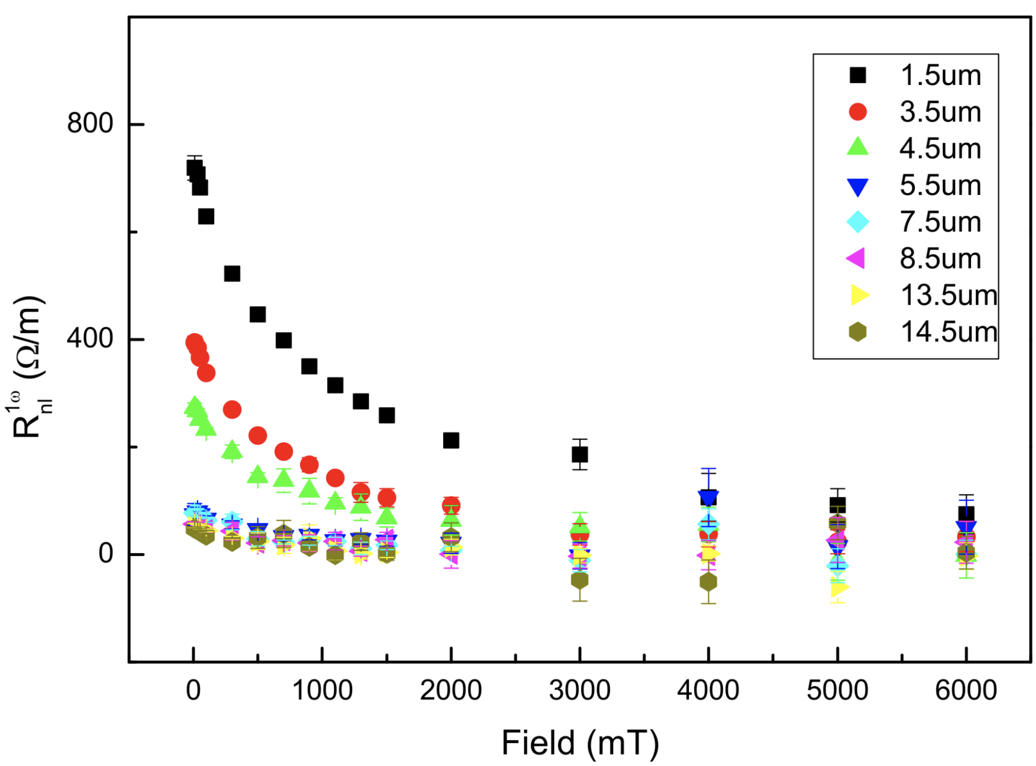

FIG. S11. The non-local resistance as function of magnetic field for $t_{\rm YIG}$ = 7.9 nm.

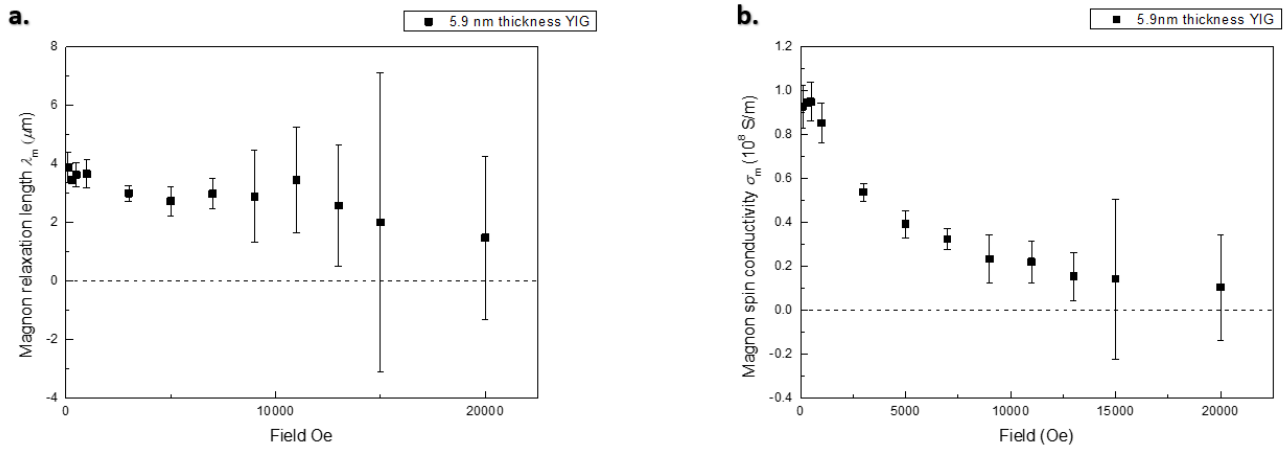

FIG. S12. λ_m and σ_m as a function of field in a film with t_{YIG} = 5.9 nm. **a)** The magnon relaxation length λ_m decreases slightly with increasing magnetic field. **b)** The magnetic field strongly suppresses the magnon conductivity σ_m..

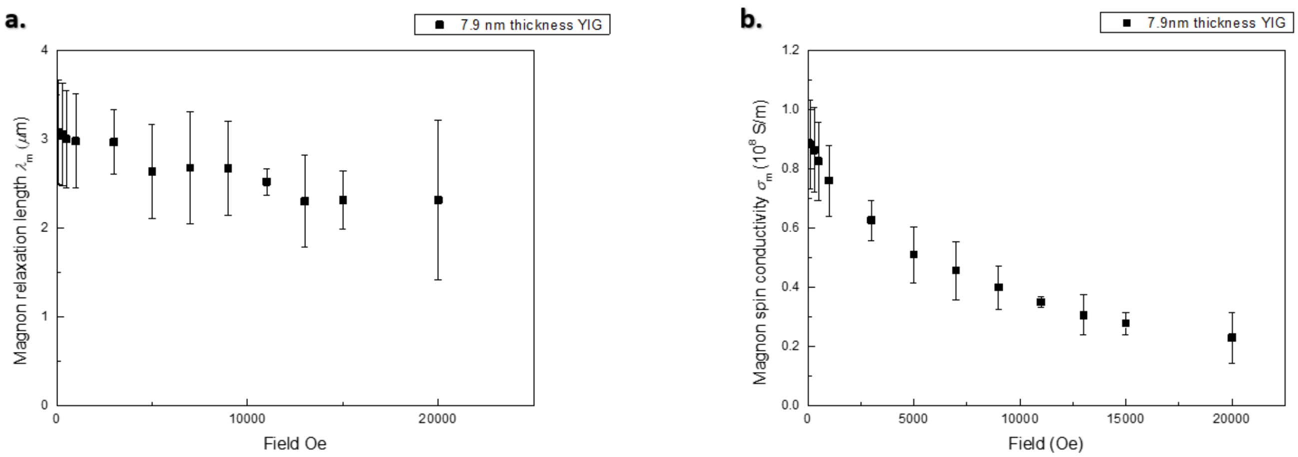

FIG. S13. **a)** λ_m and **b)** σ_m, as a function of field in a film with t_{YIG} = 7.9 nm.

VII. TEMPERATURE DEPENDENCE OF THE NON-LOCAL SIGNAL IN ULTRATHIN FILMS

We measured the temperature dependence of the non-local signal on series A samples with t_{YIG} = 3.7 nm (Figure. S14), 5.9 nm (Figure. S15) and 7.9 nm (Figure. S16) and a magnetic field of 50 mT. $R_{\mathrm{nl}}^{1\omega}$ for t_{YIG} = 3.7 nm at low temperatures is more than five times larger for d = 1.3 μm than for d = 2 μm. Since the decrease of G_s^{eff} due to the temperature is equivalent for both devices. The large change of the ratio of $R_{\mathrm{nl}}^{1\omega}$ for d = 1.3 μm and d = 2 μm suggests that $R_{\mathrm{nl}}^{1\omega}$ is dominated by the magnon spin conductivity of YIG and not the Pt|YIG interface spin conductance, which supports the conclusions from Section III.

Results of the fit by Eq. 3 from the main text are shown in Figure. S17 and Figure. S18. The magnon relaxation length only slightly changes with temperature, in contrast to that σ_m decreases strongly with temperature. In thick YIG films, $R_{\mathrm{nl}}\,(T)$ decreases slowly at high temperatures and faster at low temperatures [S10, S11], but the decrease at low temperatures is much more pronounced for ultrathin thickness YIG. Also this result is consistent with the dominant role of the lowest magnon subband in thermal transport in the thinnest films, since the two-dimensional magnon gas is more susceptible to the freeze out of carriers at low temperatures.

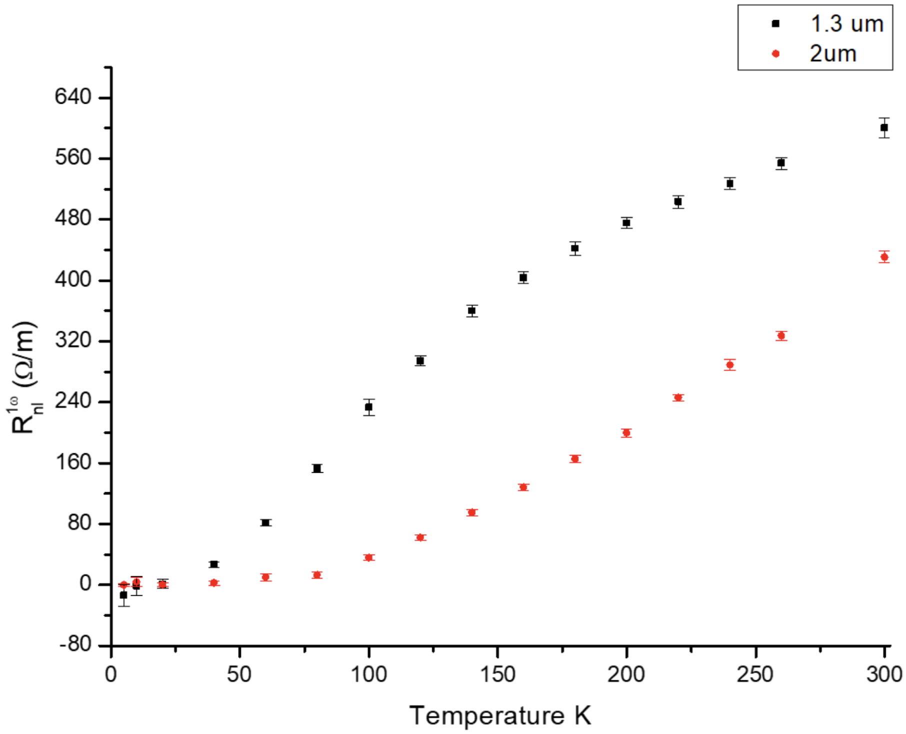

FIG. S14. The non-local resistance $R_{\mathrm{nl}}^{1\omega}$ as a function of temperature for different contact distances on a YIG film with $t_{\mathrm{YIG}} = 3.7\,\mathrm{nm}$.

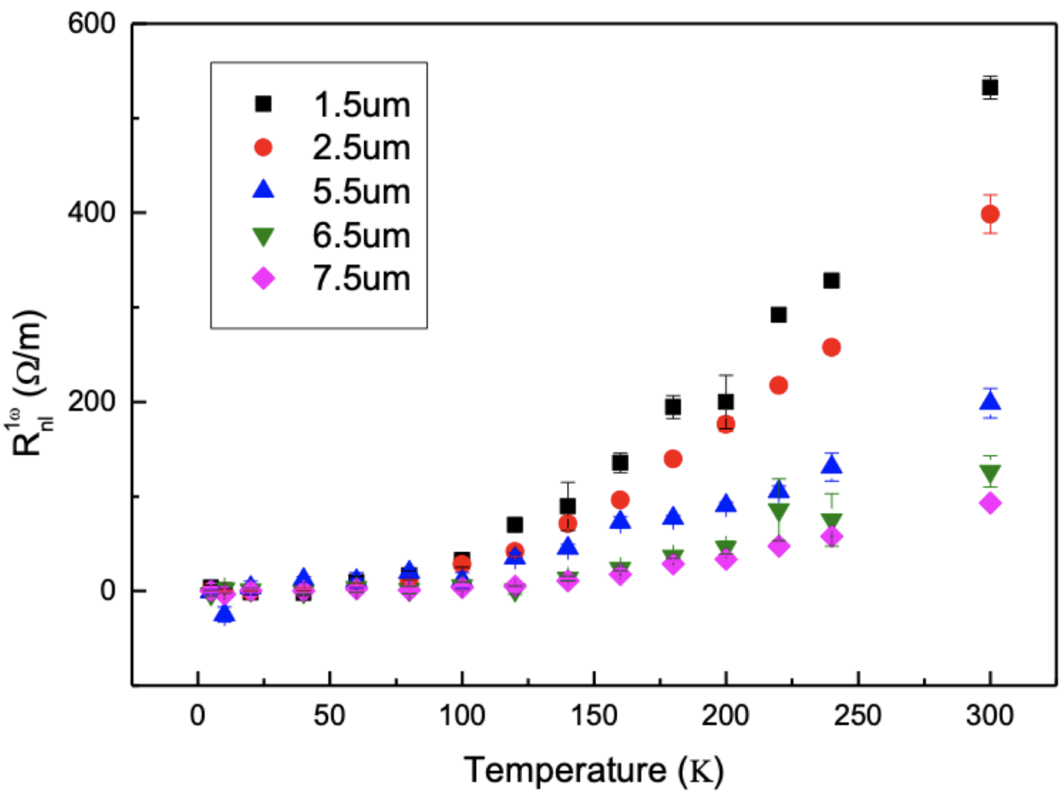

FIG. S15. Non-local resistance as a function of temperature for $t_{\mathrm{YIG}} = 5.9\,\mathrm{nm}$.

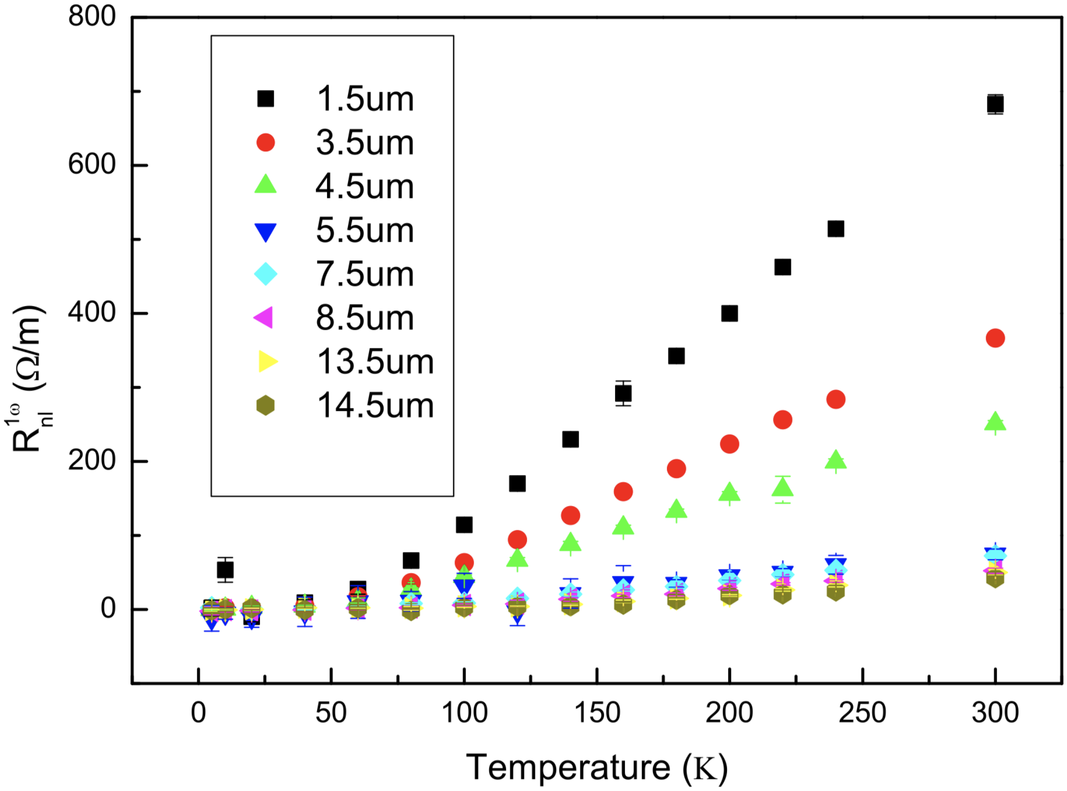

FIG. S16. Non-local resistance as a function of temperature for $t_{\mathrm{YIG}} = 7.9\,\mathrm{nm}$.

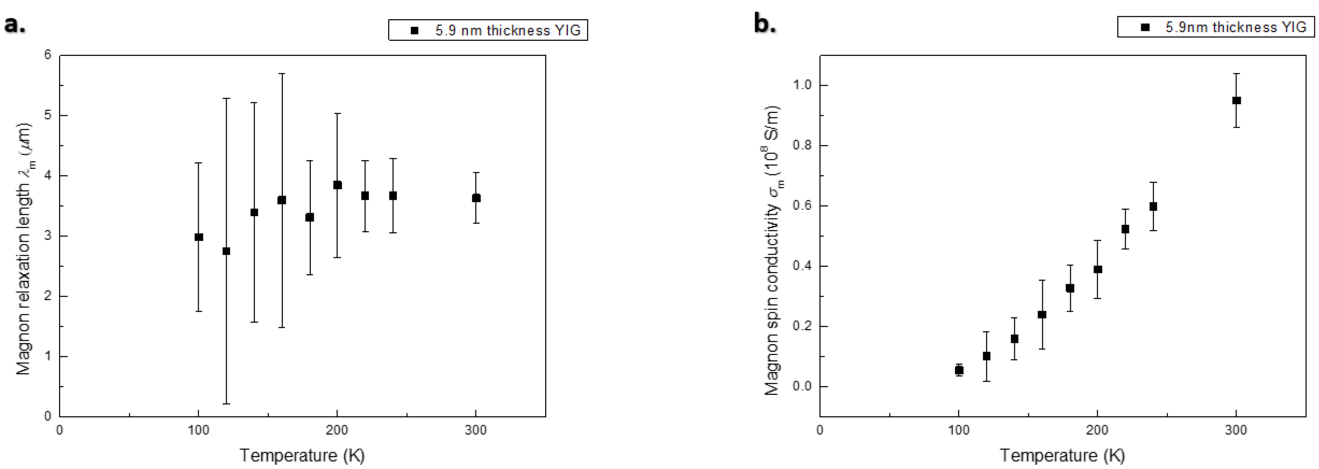

FIG. S17. **a)** λ_m and **b)** σ_m as a function of temperature for $t_{\mathrm{YIG}} = 5.9\,\mathrm{nm}$.

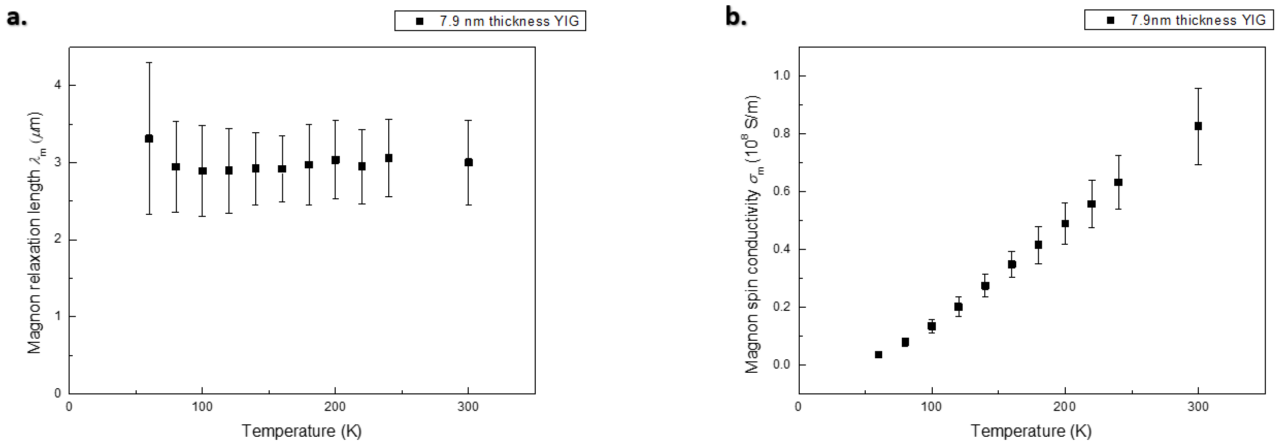

FIG. S18. **a)** λ_m and **b)** σ_m as a function of temperature for t_{YIG} = 7.9 nm.

VIII. HIGHEST OCCUPIED EXCHANGE MODE OF YIG AT ROOM TEMPERATURE

Figure. S19 shows the highest occupied exchange perpendicular standing spin waves (PSSW) 2D subbands n for different thickness YIG films at room temperature. The number of the occupied subbands is $n+1$. It is reduced from over 10^4 to a few when the thickness of the films is down to 3.7 nm.

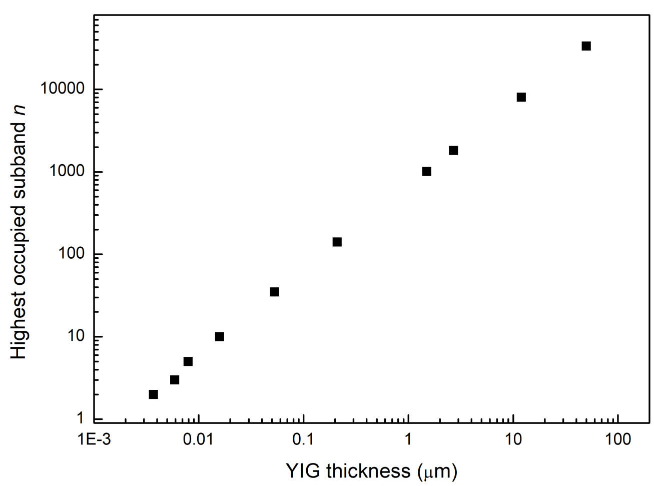

FIG. S19. Thickness dependency of the number of occupied PSSW modes defined as the highest occupied subband n at 300 K.

[S1] Sinova, J., Valenzuela, S. O., Wunderlich, J., Back, C. H. & Jungwirth, T. Spin Hall effects. *Rev. Mod. Phys.* **87**, 1213–1260 (2015).
[S2] Cornelissen, L. J., Peters, K. J. H., Bauer, G. E. W., Duine, R. A. & van Wees, B. J. Magnon spin transport driven by the magnon chemical potential in a magnetic insulator. *Phys. Rev. B* **94**, 014412 (2016).

[S3] Weiler, M. *et al.* Experimental Test of the Spin Mixing Interface Conductivity Concept. *Phys. Rev. Lett.* **111**, 176601 (2013).

[S4] Qiu, Z. *et al.* Spin mixing conductance at a well-controlled platinum/yttrium iron garnet interface. *Applied Physics Letters* **103**, 092404 (2013).

[S5] Cornelissen, L. J., Liu, J., Duine, R. A., Ben Youssef, J. & van Wees, B. J. Long-distance transport of magnon spin information in a magnetic insulator at room temperature. *Nature Physics* **11**, 1022–1026 (2015).

[S6] Shan, J. *et al.* Influence of yttrium iron garnet thickness and heater opacity on the nonlocal transport of electrically and thermally excited magnons. *Phys. Rev. B* **94**, 174437 (2016).

[S7] Kohno, R. *et al.* Enhancement of YIG |Pt spin conductance by local Joule annealing. *Applied Physics Letters* **118**, 032404 (2021).

[S8] Sierra, J. F. *et al.* Thermoelectric spin voltage in graphene. *Nature Nanotechnology* **13**, 107–111 (2018).

[S9] Shan, J. *et al.* Criteria for accurate determination of the magnon relaxation length from the nonlocal spin Seebeck effect. *Phys. Rev. B* **96**, 184427 (2017).

[S10] Cornelissen, L. J., Shan, J. & van Wees, B. J. Temperature dependence of the magnon spin diffusion length and magnon spin conductivity in the magnetic insulator yttrium iron garnet. *Phys. Rev. B* **94**, 180402 (2016).

[S11] Gomez-Perez, J. M., Vélez, S., Hueso, L. E. & Casanova, F. Differences in the magnon diffusion length for electrically and thermally driven magnon currents in $Y_3Fe_5O_{12}$. *Phys. Rev. B* **101**, 184420 (2020).